

A δf PIC method with Forward-Backward Lagrangian reconstructions

Martin Campos Pinto¹, Merlin Pelz², and Pierre-Henri Tournier³

¹Max-Planck-Institut für Plasmaphysik, Boltzmannstraße 2, D-85748 Garching b. München, Germany

²Department of Mathematics, University of British Columbia, Vancouver, British Columbia, V6T 1Z2, Canada

³Sorbonne Université, CNRS, Université de Paris, Laboratoire Jacques-Louis Lions (LJLL), F-75005 Paris, France

February 20, 2023

Abstract

In this work we describe a δf particle simulation method where the bulk density is periodically remapped on a coarse spline grid using a Forward-Backward Lagrangian (FBL) approach. This method is designed to handle plasma regimes where the densities strongly deviate from their initial state and may evolve into general profiles. We describe the method in the case of an electrostatic particle-in-cell scheme and validate its qualitative properties using a classical two-stream instability subject to a uniform oscillating drive.

1 Introduction

In order to reduce the statistical noise in numerical simulations of kinetic plasma problems, particle-in-cell (PIC) methods often follow a so-called δf approach [22, 14, 29] which consists of decomposing the transported density in two parts, a bulk density f_0 given by an analytical formula and a variation δf represented with numerical particles. In Ref. [2] this approach was revisited as a variance reduction method in the scope of Monte Carlo algorithms, with f_0 playing the role of a control variate, and since then several techniques have been devised to improve the reduction of statistical error, in particular for gyrokinetic simulation models [20, 27, 26, 19] and collisional models [8, 36, 34].

In many practical problems the plasma either remains close to an equilibrium state [20, 5], or evolves as a small perturbation of some analytically known background [23, 3, 31] which can be used as a bulk density. In some cases however the plasma evolves in an unpredictable way and f_0 needs to be updated by a self-consistent algorithm to better follow the total density.

Typical examples are problems where full- f simulations are needed. In the physics of tokamak plasmas, one instance is the modeling of $E \times B$ staircases [13] which are long-lived patterns of quasiregular step-like profiles that develop spontaneously in turbulent plasmas. As they slowly move in the radial direction over large time scales, the separation assumption between an

analytical background and fluctuations is no longer valid after some time and simulations need to involve full- f methods such as the semi-Lagrangian scheme used in the GYSELA code [18]. Another example is the modelling of the tokamak edge region where the plasma density may strongly deviate from local Maxwellian distributions, with large and intermittent fluctuations. This has motivated the development of various Eulerian full- f schemes such as those presented in Ref. [15, 25], where large plasma blob structures can be seen propagating from the core region towards the tokamak edge.

If one desires to model such problems with a δf PIC method, it is thus necessary to allow for general updates of the bulk density over time. An interesting approach in this direction was proposed in Ref. [1]: it consisted of projecting the particle density δf on a coarse spline basis and add the resulting smoothed distribution to the bulk density.

In this article we consider a variant of this approach where the bulk density is updated using a semi-Lagrangian approach based on the Forward-Backward Lagrangian (FBL) method [7].

Inspired by Ref. [12], the core of the FBL method is to compute backward trajectories on arbitrary nodes by local inversions of the particle trajectories: as these describe the forward transport flow in phase space and are naturally provided by the PIC code, their local inversion allows to perform semi-Lagrangian updates of a smooth density represented on a coarse grid. In particular the novelty of our approach is that it does not primarily rely on an accurate particle approximation of the density itself, but rather on an accurate description of the particle trajectories. As these are in general much less noisy than the phase space density, we believe that this new paradigm can lead to efficient low-noise particle methods.

The outline is as follows. In Section 2 we present our general ansatz for the discrete density, which may be seen as a hybrid discretization between particle and semi-Lagrangian density representations. In Section 3 we recall the key steps of electrostatic particle-in-cell approximations, and in Section 4 we describe the δf PIC method with FBL remappings of the bulk density. The proposed method is summarized in Section 5, and in Section 6 we present a series of numerical results involving two-stream instability test cases to illustrate the enhanced denoising properties of our approach. We conclude in Section 7 with a summary of the proposed method, a discussion on its novelty and two perspectives for future research.

2 Approximation ansatz

Our ansatz for the general density at a discrete time t^n is a sum of two terms,

$$f^n := f_*^n + \delta f^n \tag{1}$$

(we shall often use $:=$ to highlight a definition) where the first one will be seen as the bulk density, a smooth approximation to the full solution, and the second one as the fine scale variations. Following the general principle of δf methods we require f_*^n to have a simple expression that is easy to evaluate at arbitrary positions in a general d -dimensional phase space, and we represent the variation δf^n as an unstructured collection of numerical particles with coordinates z_k^n and weights δw_k^n ,

$$\delta f^n(z) := \sum_{k=1}^{N_p} \delta w_k^n \varphi_\varepsilon(z - z_k^n). \tag{2}$$

Here φ_ε is a smooth shape function of scale ε and $z = (z_1, \dots, z_d)$ is a phase-space coordinate. In typical problems where the transported density slightly deviates from an initial profile, the

bulk density is often set to this initial value, $f_*^n = f^0$ or to some analytical equilibrium [20, 5]. In this note we investigate an alternate approach where the bulk density is represented as an arbitrary collection of B-splines on a coarse grid with mesh-size $h_* > \varepsilon$, in the spirit of Ref. [1]. This yields an expression that is formally similar to that of δf^n ,

$$f_*^n(z) = \sum_{j \in \mathbb{Z}^d} w_{*,j}^n \varphi_{h_*}(z - jh_*) \quad (3)$$

where $\varphi_*(\cdot - jh_*)$ is now the coarse B-spline shape centered on a general d -dimensional grid node jh_* (\mathbb{Z} is the set of integers) and $w_{*,j}^n$ is its weight. In practice, only a finite number N_* of such nodes is used, and as outlined in the introduction we will periodically update the coefficients of this spline bulk density using a Forward-Backward Lagrangian (FBL) reconstructions, which involves a relatively small set of passive markers designed to track the characteristic flow in phase space.

2.1 Main numerical parameters and limit regimes

The main numerical parameters are as follows.

- N_r is the remapping period, i.e., the number of time steps between two updates of the bulk density. The limit value $N_r = \infty$ corresponds to a frozen bulk density, namely $f_*^n = f_*^0$ for every time step n .
- N_* is the number of coarse splines used to represent the bulk density in the computational domain $\Omega \subset \mathbb{R}^d$, it is on the order of $\text{Vol}(\Omega)(h_*)^{-d}$. The limit value of $N_* = 0$ (an empty grid) corresponds to a “full- f ” particle approximation.
- N_p is the number of numerical particles describing the fine scale structures. The limit value of $N_p = 0$ corresponds to a semi-Lagrangian ansatz [33] where the full density is represented on a structured grid and can be updated in time with an ad-hoc scheme such as the FBL method described in Ref. [7].

2.2 Weighted collections of spline shape functions

For simplicity, we consider spline shape functions for both the bulk density and the fine scale variations. Specifically, we set

$$\varphi_\varepsilon(z) := \left(\frac{1}{\varepsilon}\right)^d \varphi\left(\frac{z}{\varepsilon}\right), \quad z \in \mathbb{R}^d$$

with a reference shape function φ defined as a centered cardinal B-spline of degree p ,

$$\varphi(z) := \prod_{i=1}^d B_p(z_i) \quad \text{with support} \quad \left[-\frac{p+1}{2}, \frac{p+1}{2}\right]^d$$

involving standard univariate B-splines defined recursively by

$$B_0(x) := \mathbb{1}_{\left[-\frac{1}{2}, \frac{1}{2}\right]}(x) \quad \text{and} \quad B_p(x) := \int_{x-\frac{1}{2}}^{x+\frac{1}{2}} B_{p-1} \quad \text{for } p \geq 1.$$

In the sequel, it will be convenient to denote an arbitrary collection of weighted splines as

$$\Phi_\varepsilon[\mathbf{W}, \mathbf{Z}](z) := \sum_{k=1}^N w_k \varphi_\varepsilon(z - z_k)$$

where $\mathbf{W} = (w_k)_{k=1\dots N}$, $\mathbf{Z} = (z_k)_{k=1\dots N}$. With this convention, the two components of our general ansatz (1) read

$$f_*^n = \Phi_{h_*}[\mathbf{W}_*^n, \mathbf{Z}_*] \quad \text{and} \quad \delta f^n = \Phi_\varepsilon[\delta \mathbf{W}^n, \mathbf{Z}^n] \quad (4)$$

where $\mathbf{Z}_* := (j h_*)_{j \in \mathbb{Z}^d}$ are the nodes of the spline grid.

3 Particle approximations to transport equations

Our method may be described for general non-linear transport problems of the form

$$\partial_t f(t, z) + U[f] \cdot \nabla_z f(t, z) = 0 \quad (5)$$

where $z \in \mathbb{R}^d$ is the phase-space variable and $U[f]$ the generalized velocity field associated to the solution f .

3.1 Characteristic flows

The characteristic trajectories associated to Eq. (5) are the curves $Z(t) = Z(t; s, z) \in \mathbb{R}^d$, solution to the ODEs

$$\frac{d}{dt} Z(t) = U[f](t, Z(t)), \quad Z(s) = z$$

for arbitrary $s, t \in [0, T]$ and $z \in \mathbb{R}^d$, see e.g. Ref. [30]. The (forward) characteristic flow between two times $t^n = n\Delta t$ and $t^{n+1} = (n+1)\Delta t$ is then defined as

$$\mathcal{F}_{\text{ex}}^{n, n+1}(z) := Z(t^{n+1}; t^n, z) \quad (6)$$

and the inverse mapping $\mathcal{B}_{\text{ex}}^{n, n+1} := (\mathcal{F}_{\text{ex}}^{n, n+1})^{-1}$ is the backward flow

$$\mathcal{B}_{\text{ex}}^{n, n+1}(z) = Z(t^n; t^{n+1}, z). \quad (7)$$

Using the backward flow we can write the solution to Eq. (5) over the time interval $[t^n, t^{n+1}]$ as

$$f(t^{n+1}, z) = f(t^n, \mathcal{B}_{\text{ex}}^{n, n+1}(z)). \quad (8)$$

Here we may restrict ourselves to divergence-free velocity fields: $\text{div}_z U[f] = 0$. The characteristic flows are then measure-preserving and the transport is conservative.

3.2 1D1V Vlasov-Poisson equation

A simple example is the periodic Vlasov-Poisson equation in a two dimensional phase-space, i.e., $z = (x, v)$ with a periodic space coordinate $x \in [0, L]$ and velocity $v \in \mathbb{R}$

$$\partial_t f(t, x, v) + v \partial_x f(t, x, v) - E(t, x) \partial_v f(t, x, v) = 0 \quad (9)$$

for $t \geq 0$, $(x, v) \in [0, L] \times \mathbb{R}$, with a normalized initial density $\int_0^L \int_{\mathbb{R}} f^0(x, v) dv dx = 1$ and a periodic electric field $E = E[f]$ defined by

$$\begin{cases} E(t, x) = -\partial_x \phi(t, x) \\ -\Delta \phi(t, x) = \rho(t, x) = \frac{1}{L} - \int_{\mathbb{R}} f(t, x, v) dv. \end{cases} \quad (10)$$

This corresponds to an electrostatic, normalized ($\varepsilon_0 = q_e = m = 1$) periodic electron plasma in 1D, with constant neutralizing background ion density, so that $\int_0^L \rho dx = 0$. Here the generalized velocity field is

$$U[f](t, z) = (v, -E(t, x)) \quad \text{with } z = (x, v).$$

Due to the non-linear nature of this transport equation, the characteristic flow has no explicit expression.

3.3 Full- f particle approximation

Particle approximations represent the transported density $f^n(z) \approx f(t^n, z)$ as a sum of numerical particles of the form

$$f^n(z) = \Phi_\varepsilon[\mathbf{W}^n, \mathbf{Z}^n](z) \quad (11)$$

with weights initially set to

$$w_k^0 := \frac{f^0(z_k^0)}{N_p g^0(z_k^0)}, \quad k = 1, \dots, N_p, \quad (12)$$

where g^0 is the sampling distribution of the initial markers $\mathbf{Z}^0 = (z_k^0)_{k=1, \dots, N_p}$, see e.g. Ref. [34]. As the problem is conservative the weights are kept constant in time, $\mathbf{W}^{n+1} = \mathbf{W}^n$, and the markers are pushed forward

$$\mathbf{Z}^{n+1} = \mathcal{F}^n(\mathbf{Z}^n) \quad (13)$$

using some approximation to the forward flow in Eq. (6) which takes as parameter the numerical solution at time t^n ,

$$\mathcal{F}^n(\mathbf{Z}) = \mathcal{F}_{\Delta t}[\mathbf{W}^n, \mathbf{Z}^n](\mathbf{Z}).$$

3.4 Electrostatic full- f leap-frog flow

For the Vlasov-Poisson equation (9), a standard numerical flow is given by a leap-frog (Strang splitting) scheme,

$$\mathcal{F}_{\Delta t, \Delta x}^{\text{lf, pic}}[\mathbf{W}^n, \mathbf{Z}^n](\mathbf{Z}) = \mathcal{F}_{\frac{\Delta t}{2}}^x \circ \mathcal{F}_{\Delta t, \Delta x}^{\text{v, pic}}[\mathbf{W}^{n+\frac{1}{2}}, \mathbf{Z}^{n+\frac{1}{2}}] \circ \mathcal{F}_{\frac{\Delta t}{2}}^x(\mathbf{Z}) \quad (14)$$

(where \circ is the usual function composition operator) associated with a grid with M points and step-size $\Delta x = L/M$. The first split flow reads

$$\mathcal{F}_{\frac{\Delta t}{2}}^x(x, v) := \left(x + \frac{\Delta t}{2}v, v\right) \quad (15)$$

and the second one takes the form

$$\mathcal{F}_{\Delta t, \Delta x}^{\text{v,pic}}[\mathbf{W}^{n+\frac{1}{2}}, \mathbf{Z}^{n+\frac{1}{2}}](x, v) := (x, v - \Delta t E^{n+\frac{1}{2}}(x)). \quad (16)$$

Here we have set

$$\mathbf{W}^{n+\frac{1}{2}} := \mathbf{W}^n, \quad \mathbf{Z}^{n+\frac{1}{2}} := \mathcal{F}_{\frac{\Delta t}{2}}^x(\mathbf{Z}^n) \quad (17)$$

and the electric field is computed from the particles with a discrete Poisson solver such as the one described just below, that takes as input the particle weights and positions,

$$E^{n+\frac{1}{2}}(x) := \mathbf{E}_{\Delta x}^{\text{pic}}[\mathbf{W}^{n+\frac{1}{2}}, \mathbf{Z}^{n+\frac{1}{2}}](x). \quad (18)$$

3.5 Electrostatic full- f PIC field solver

To clarify how the particles are coupled with the field in Eq. (18), we recall the precise form of a basic Finite Difference (FD) Poisson solver for a general collection of weighted particles, i.e.,

$$\Phi_\varepsilon[\mathbf{W}, \mathbf{Z}] \mapsto \mathbf{E}_{\Delta x, \varepsilon}^{\text{pic}}[\mathbf{W}, \mathbf{Z}]. \quad (19)$$

We note that for periodic systems spectral solvers involving fast Fourier transforms are often used, see e.g. Ref. [4, Sec. 8]. In both cases the charge deposition algorithm consists of computing grid values for the charge density,

$$\rho_i = \frac{1}{L} - \int_{\mathbb{R}} \Phi_\varepsilon[\mathbf{W}, \mathbf{Z}](i\Delta x, v) dv = \frac{1}{L} - \sum_{k=1}^{N_p} w_k \varphi_\varepsilon(i\Delta x - x_k) \quad (20)$$

for $i = 1, \dots, M$. A discrete Poisson equation is then solved. With a FD scheme this reads

$$E_i = -\frac{\phi_{i+1} - \phi_{i-1}}{2\Delta x}, \quad -\frac{\phi_{i+1} - 2\phi_i + \phi_{i-1}}{\Delta x^2} = \rho_i,$$

for $i = 1, \dots, M$. The electric field (19) is then defined using the same spline shape functions as the particles but a different normalization, and scaled with the FD grid:

$$\mathbf{E}_{\Delta x, \varepsilon}^{\text{pic}}(x) := \sum_{i=1}^M E_i \tilde{\varphi}_{\Delta x}(x - i\Delta x) \quad \text{where} \quad \tilde{\varphi}_{\Delta x}(x) = \varphi\left(\frac{x}{\Delta x}\right).$$

In the usual case where $\varepsilon = \Delta x$, we write $\mathbf{E}_{\Delta x}^{\text{pic}} = \mathbf{E}_{\Delta x, \Delta x}^{\text{pic}}$.

4 A δf PIC scheme with remappings

We now describe the main steps of a δf method involving a decomposition of the form Eq. (1). Denoting by N_r the remapping period, we first observe that the bulk part is frozen between two remapping steps. This yields in particular

$$f_*^n = f_*^m \quad \text{where} \quad m = m(n) := \left\lfloor \frac{n}{N_r} \right\rfloor N_r. \quad (21)$$

The δf part is then evolved as follows.

4.1 δf particle approximation: basic steps

A typical δf time step consists of (i) pushing the markers forward to follow the characteristic curves as in Eq. (13),

$$\mathbf{Z}^{n+1} = \mathcal{F}^n(\mathbf{Z}^n) \quad (22)$$

and (ii) updating the weights. Indeed, since the numerical particles now represent a variation $\delta f^n = f^n - f_*^n$ with frozen f_*^n on the time step, their weights no longer carry a conserved density and they must be evolved in time. In the *direct* δf method (see e.g. Ref. [34, Sec. 3]) they are set as

$$\delta w_k^n := \frac{f_k^n - f_*^n(z_k^n)}{N_p g_k^n} \approx \frac{\delta f(t^n, z_k^n)}{N_p g(t^n, z_k^n)}, \quad k = 1, \dots, N_p \quad (23)$$

where

$$f_k^n \approx f(t^n, z_k^n) \quad \text{and} \quad g_k^n \approx g(t^n, z_k^n) \quad (24)$$

correspond to the transported density and the markers density probability, respectively, evaluated at the particle positions. Since both values are constant along exact trajectories, a reasonable choice is

$$f_k^n := f^0(z_k^0) \quad \text{and} \quad g_k^n := g^0(z_k^0). \quad (25)$$

Up to these constant values we see that the δf weights only depend on the bulk density, which is characterized by the weights $\mathbf{W}_*^n = \mathbf{W}_*^m$, at the marker positions \mathbf{Z}^n . Hence we may summarize the weighting scheme in Eq. (23)–(25) as

$$\delta \mathbf{W}^n := \delta \mathcal{W}(\mathbf{W}_*^m, \mathbf{Z}^n). \quad (26)$$

4.2 Electrostatic δf -PIC flow

In the case of a δf ansatz, the leap-frog flow reads

$$\mathcal{F}_{\Delta t, \Delta x}^{\text{lf}, \delta f}[\mathbf{W}_*^m, \mathbf{Z}^n] = \mathcal{F}_{\frac{\Delta t}{2}}^x \circ \mathcal{F}_{\Delta t, \Delta x}^{\text{v}, \delta f}[\mathbf{W}_*^m, \mathbf{Z}^{n+\frac{1}{2}}] \circ \mathcal{F}_{\frac{\Delta t}{2}}^x \quad (27)$$

with split flows defined similarly as in Eq. (15)–(16) and a field solver adapted to the ansatz from Eq. (1), namely

$$\mathcal{F}_{\Delta t, \Delta x}^{\text{v}, \delta f}[\mathbf{W}_*^m, \mathbf{Z}^{n+\frac{1}{2}}](x, v) := (x, v - \Delta t E^{n+\frac{1}{2}}(x)) \quad (28)$$

with

$$E^{n+\frac{1}{2}} = E_*^m + E_{\delta f}^{n+\frac{1}{2}} = \mathbf{E}_{\Delta x, h_*}[\mathbf{W}_*^m, \mathbf{Z}^{n+\frac{1}{2}}]. \quad (29)$$

Since both parts of the density are formally written as weighted collections of spline shapes, we may use a standard PIC solver for each parts. The field induced by the bulk density f_*^m is

$$E_*^m := \mathbf{E}_{\Delta x, h_*}^{\text{pic}}[\mathbf{W}_*^m, \mathbf{Z}_*] \quad (30)$$

and the field corresponding to the variation $\delta f^{n+\frac{1}{2}} = \Phi_\varepsilon[\delta \mathbf{W}^{n+\frac{1}{2}}, \mathbf{Z}^{n+\frac{1}{2}}]$, with scaling $\varepsilon = \Delta x$, reads

$$E_{\delta f}^{n+\frac{1}{2}} = \mathbf{E}_{\Delta x}^{\text{pic}}[\delta \mathbf{W}^{n+\frac{1}{2}}, \mathbf{Z}^{n+\frac{1}{2}}]$$

$$\text{with} \quad \begin{cases} \delta \mathbf{W}^{n+\frac{1}{2}} := \delta \mathcal{W}(\mathbf{W}_*^m, \mathbf{Z}^{n+\frac{1}{2}}) \\ \mathbf{Z}^{n+\frac{1}{2}} := \mathcal{F}_{\frac{\Delta t}{2}}^x(\mathbf{Z}^n) \end{cases} \quad (31)$$

see (17), (26), (23). The resulting field solver corresponding to (29) may then be written as

$$\begin{aligned} \mathbb{E}_{\Delta x, h_*}[\mathbf{W}_*^m, \mathbf{Z}^{n+\frac{1}{2}}] &:= \mathbb{E}_{\Delta x, h_*}^{\text{bic}}[\mathbf{W}_*^m, \mathbf{Z}_*] \\ &\quad + \mathbb{E}_{\Delta x}^{\text{pic}}[\delta\mathcal{W}(\mathbf{W}_*^m, \mathbf{Z}^{n+\frac{1}{2}}), \mathbf{Z}^{n+\frac{1}{2}}]. \end{aligned}$$

Since the field E_*^m is constant between two remappings, regular time steps only involve a deposition of the δf particles to update the $E_{\delta f}$ part. Note that even if $|\delta f^n| \ll |f_*^m|$, there is no reason why $E_{\delta f}$ should be small compared to E_*^m . In particular, we have $E_*^m \approx 0$ when f_*^m is close to an equilibrium density.

4.3 FBL remappings with auxiliary markers

For the remappings, namely the updates of the bulk density $f_*^m \mapsto f_*^n$ with $n = m + N_r$, we resort to Forward-Backward Lagrangian (FBL) reconstructions [7]. As mentioned above this involves a collection of auxiliary markers that have been reset on the Cartesian grid at the previous remapping step,

$$\tilde{\mathbf{Z}}^m := \mathbf{Z}_*, \quad \text{i.e.,} \quad \tilde{z}_j^m := \mathbf{j}h_* \quad \forall \mathbf{j} \in \mathbb{Z}^d, \quad (32)$$

and pushed forward similarly as the classical ones in Eq. (22),

$$\tilde{\mathbf{Z}}^n = \mathcal{F}^{n-1}(\dots \mathcal{F}^m(\mathbf{Z}_*) \dots) \quad (33)$$

in order to track the forward characteristic flow. The FBL method then performs a semi-Lagrangian step

$$f_*^n := A_* \mathcal{T}_{\text{fbl}}[\tilde{\mathbf{Z}}^n] f_*^m \quad (34)$$

where A_* is a spline interpolation or quasi-interpolation operator on the h_* grid, and $\mathcal{T}_{\text{fbl}}[\tilde{\mathbf{Z}}^m] : f \mapsto f \circ \mathcal{B}_{\text{fbl}}^{m,n}$ is a transport operator approximating the exact one in Eq. (8), based on an FBL backward flow

$$\mathcal{B}_{\text{fbl}}^{m,n} = \mathcal{B}_{\text{fbl}}[\tilde{\mathbf{Z}}^n] \approx \mathcal{B}_{\text{ex}}^{m,n}. \quad (35)$$

As a result we obtain a numerical scheme to update the coefficients of the bulk density, which we summarize as

$$\mathbf{W}_*^n := \text{Remap}[\tilde{\mathbf{Z}}^n](\mathbf{W}_*^m) \quad (36)$$

where n is a multiple of N_r and $m = n - N_r$.

In the next subsection we give some details about the FBL algorithm.

4.4 FBL density reconstructions

The FBL scheme in Eq. (34) performs a semi-Lagrangian approximation with a backward flow derived from the position of the auxiliary markers $\tilde{\mathbf{Z}}^m$ in Eq. (33), as follows:

- (i) For any index $\mathbf{j} \in \mathbb{Z}^d$, let \tilde{z}_i^m with $\mathbf{i} = \mathbf{i}(\mathbf{j})$ be an FBL marker close to the node $\mathbf{j}h_*$
- (ii) Compute the quadratic local backward flow associated with \tilde{z}_i^m , namely

$$B_i^{m,n}(z) = z_i^* + D_i^n(z - \tilde{z}_i^m) + \frac{1}{2}(z - \tilde{z}_i^m)^T Q_i^n(z - \tilde{z}_i^m) \quad (37)$$

where $z_i^* = \mathbf{i}h_*$, and where D_i^n , Q_i^n correspond respectively to the Jacobian matrix and Hessian tensor of the backward flow at $z = \tilde{z}_i^m$, computed from the positions of the logical neighbors of \tilde{z}_i^m (for more details see Ref. [7])

(iii) Reconstruct the transported density at node $z_j^* = \mathbf{j}h_*$ using this approximated flow,

$$f_{*,\mathbf{j}}^n := f_*^m(B_{\mathbf{i}}^{m,n}(z_j^*)) \quad (38)$$

(iv) Compute the new weights \mathbf{W}_*^n using a spline approximation operator A^* .

For the operator A_* , we can use a standard interpolation scheme, or even a local quasi-interpolation scheme, see, e.g., Ref. [10]. Both compute high-order B-spline approximations, but the latter only involves local pointwise evaluations of the target function. The resulting approximation takes the form

$$\begin{aligned} A_*g(z) &:= \sum_{\mathbf{j} \in \mathbb{Z}^d} w_{\mathbf{j}}(g) \varphi_{h_*}(z - \mathbf{j}h_*) \\ \text{with } w_{\mathbf{j}}(g) &:= h_*^d \sum_{\|\mathbf{i}\|_{\infty} \leq s_p} a_{\mathbf{i}} g((\mathbf{j} + \mathbf{i})h_*), \end{aligned} \quad (39)$$

with coefficients $a_{\mathbf{i}} := a_{i_1} \cdots a_{i_d}$ on a local stencil of size s_p , as given by the symmetric method ($a_{\mathbf{i}} = a_{-\mathbf{i}}$) in Ref. [10, Sec. 6].

5 Overview of the δf particle scheme with FBL remappings

Gathering the above steps, we may write the solution at time t^n as

$$f^n = f_*^m + \delta f^n \quad \text{with} \quad \begin{cases} f_*^m = \Phi_{h_*}[\mathbf{W}_*^m, \mathbf{Z}_*] \\ \delta f^n = \Phi_{\varepsilon}[\delta \mathbf{W}^n, \mathbf{Z}^n]. \end{cases} \quad (40)$$

Here we remind that $\mathbf{Z}_* = (\mathbf{j}h_*)_{\mathbf{j} \in \mathbb{Z}^d}$ are the coarse grid nodes and $m = m(n)$ is the last remapping step preceding n , see Eq. (21). The proposed scheme reads then as follows.

5.1 Initialization

- Compute the weights \mathbf{W}_*^0 of the initial bulk density $f_*^0 = \Phi_{h_*}[\mathbf{W}_*^0, \mathbf{Z}_*]$ with

$$f_*^0 := A_*f^0$$

using a spline approximation scheme such as the one in Eq. (39),

- Draw the δf markers according to some initial sampling distribution

$$\mathbf{Z}^0 \sim g^0$$

- Initialize the auxiliary FBL markers on the h_* grid (32),

$$\tilde{\mathbf{Z}}^0 := \mathbf{Z}_* .$$

5.2 Time loop

For $n = 0, \dots, N_t - 1$, let $m := \lfloor \frac{n}{N_r} \rfloor N_r$ denote the previous remapping step as in Eq. (21), and do:

- If $n = m > 0$, **remap**:

- ▷ Update the bulk density weights (coefficients) with the FBL method described in Section 4.4,

$$\mathbf{W}_*^m := \text{Remap}[\tilde{\mathbf{Z}}^m](\mathbf{W}_*^{\hat{m}}) \quad (41)$$

- ▷ Reset the FBL markers with (32), $\tilde{\mathbf{Z}}^m := \mathbf{Z}_*$

- **Push** the markers forward:

$$\begin{cases} \mathbf{Z}^{n+1} := \mathcal{F}^n(\mathbf{Z}^n) \\ \tilde{\mathbf{Z}}^{n+1} := \mathcal{F}^n(\tilde{\mathbf{Z}}^n) \end{cases} \quad (42)$$

using some discrete flow $\mathcal{F}^n = \mathcal{F}_{\Delta t}^{\delta f}[\mathbf{W}_*^m, \mathbf{Z}^n]$ such as the leap-frog scheme in Eq. (27), which involves deposition and field solver steps as detailed in Section 4.2 and 3.5.

5.3 FBL variant

A semi-Lagrangian FBL variant of the above scheme can be obtained by (i) setting $N_p = 0$ and (ii) treating the FBL markers $\tilde{\mathbf{Z}}^n$ as “active” particles in the field solver.

Specifically, this amounts to discarding the δf part ($\mathbf{Z}^n = \emptyset$) so that the full density is represented on the structured spline grid on the successive remapping steps, and to defining the electric field in Eq. (27)–(28) by

$$E^{n+\frac{1}{2}} = \mathbf{E}_{\Delta x}^{\text{pic}}[\mathbf{W}_*^{n+\frac{1}{2}}, \tilde{\mathbf{Z}}^{n+\frac{1}{2}}] \quad (43)$$

as one would do with a standard full- f PIC scheme, see (16)–(18), using the weighted FBL markers as standard particles. Note that here the weights are those set at the last remapping step (41), i.e., $\mathbf{W}_*^{n+\frac{1}{2}} = \mathbf{W}_*^m$ with m as in (21).

6 Numerical results

In this section we assess the proposed method on the periodic 1D1V Vlasov-Poisson system (9)–(10), where we compare it with other PIC and semi-Lagrangian schemes.

6.1 Numerical parameters for the tested methods

For the purpose of comparison, we use different values for the main parameters listed in Section 2.1, including some limiting values which allows to emulate full- f and δf PIC schemes, as well as a semi-Lagrangian FBL scheme. All the methods use cubic splines for the particle shape functions.

As the solutions are typically supported in a region occupying roughly one half of the computational phase-space domain, for each grid resolution $N_x \times N_v$ we indicate as $N_*^{\text{eff}} \approx N_*/2$, with

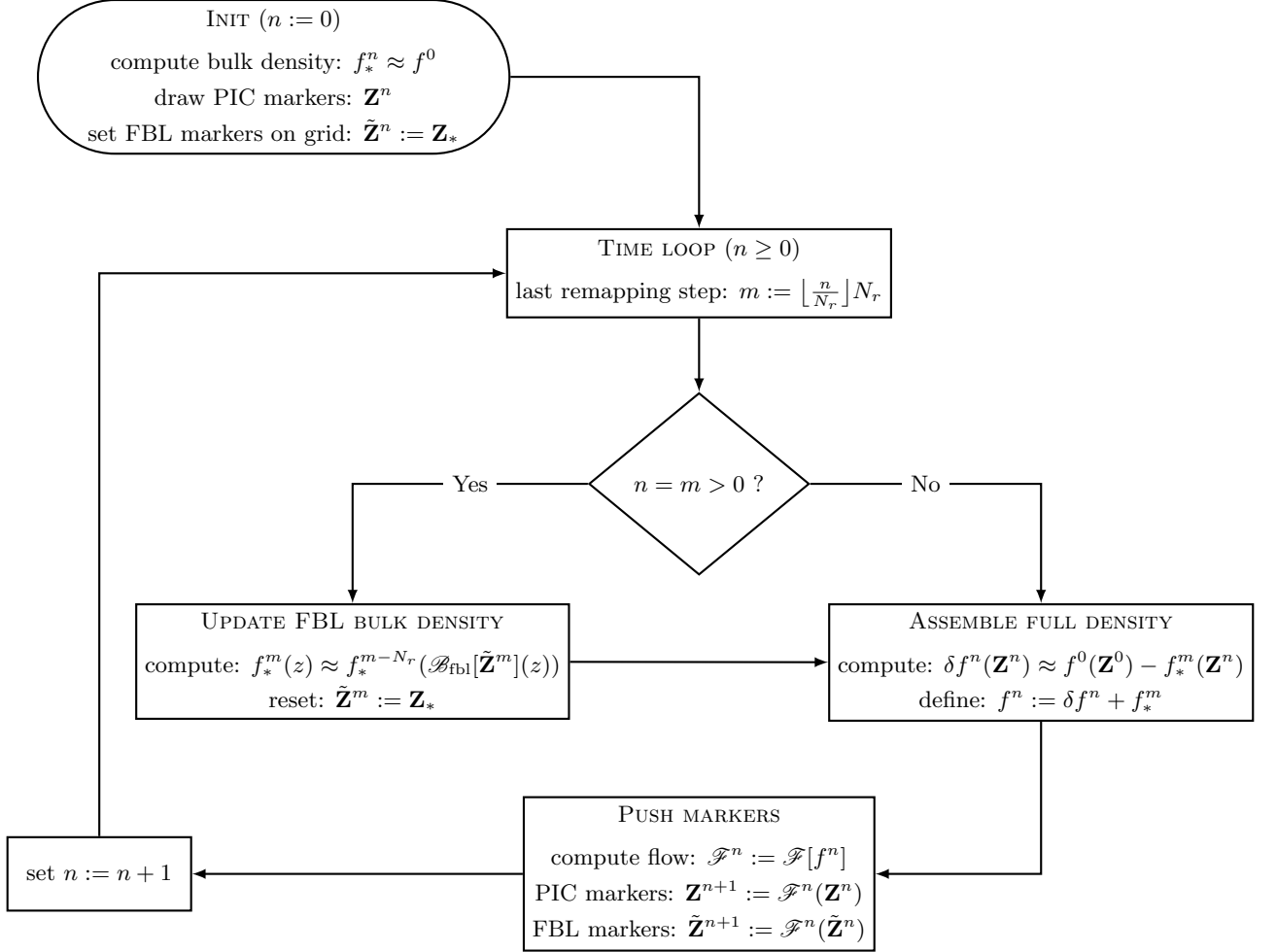


Figure 1: Flowchart summarizing the main steps of the FBL- δf scheme.

Table 1: Numerical parameters used for the different methods, as described in the text.

method	N_p	grid (FBL)	N_*^{eff}	N_r	FBL markers
full- f PIC, coarse	20,000	0×0	0	∞	\emptyset
full- f PIC, fine	320,000	0×0	0	∞	\emptyset
δf PIC	18,752	50×50	1,250	∞	frozen
FBL, coarse	0	200×200	20,000	20	active
FBL, fine	0	800×800	320,000	20	active
FBL- δf PIC	18,752	50×50	1,250	20	passive

$N_* = N_x N_y$, the approximate number of active spline coefficients on the grid, corresponding to the “effective” grid resolution. The resulting methods are summarized in Table 1.

Here the active/passive/frozen status of FBL markers $\tilde{\mathbf{Z}}^n$ refers to their role in the scheme and in particular in the field solver that is involved in the push step in Eq. (42): *active* markers (used in the FBL variant) carry a charge which is deposited as explained in Section 5.3 while *passive* markers (used in the proposed FBL- δf scheme) do not, as described in Section 4.2. Finally *frozen* markers are passive, and never pushed: in the absence of remappings only their initial position on the grid is used to represent the bulk density $f_*^n = f_*^0$.

We point out that in this study we do not attempt to assess the computational cost of the various methods, as the problems are academic and our implementation is far from being optimal. In particular one should keep in mind that full- f and basic δf methods, even if noisier, may be quicker to run and easier to parallelise than their FBL counterparts. Efficient implementations of the latter are left for future works.

6.2 Test cases

Our numerical experiments are based on a 1D1V two-stream instability test case where the initial distribution is of the form

$$f^0(x, v) = (1 + \alpha \cos(kx)) \frac{v^2}{\sqrt{2\pi}} e^{-\frac{v^2}{2}} \quad (44)$$

with a wave number of $k = \frac{1}{2}$ and a perturbation amplitude of $\alpha = 0.01$. This solution is known to develop thin filaments in the phase space that are difficult to resolve numerically, see, e.g., Refs. [9, 32]. Here we will simulate two-stream instabilities on the time interval $[0, 100]$. We shall consider two versions of the problem:

- (i) the basic Two-Stream Instability (TSI) test case where the solution is evolved with the self-consistent Vlasov-Poisson system (9)–(10)
- (ii) a Driven Two-Stream Instability (DTSI) test case where an oscillating external field

$$E_{\text{ext}}(t, x) = \frac{1}{10} \cos\left(\frac{\pi t}{50}\right) \quad (45)$$

is added to the self-consistent field from Eq. (10). The effect of this external drive is to add a periodic perturbation to the TSI trajectories, uniform in x and v ,

$$(x, v) \mapsto \left(x + \frac{250}{\pi^2} \left(1 - \cos \left(\frac{\pi t}{50} \right) \right), y + \frac{5}{\pi} \sin \left(\frac{\pi t}{50} \right) \right),$$

so that the solutions to both test cases coincide for $t = 100$.

The computational phase-space domain is set to

$$\Omega = [0, L] \times [-v_{\max}, v_{\max}]$$

with $L = \frac{2\pi}{k}$ and $v_{\max} = 10$. Note that this value is significantly larger than what is usually seen in the literature, in order to correctly represent the variations in velocity induced by the oscillating drive. Finally the initial sampling distribution for the particles is taken as $g^0 = (\int f^0(z) dz)^{-1} f^0$ for the full- f PIC scheme, and as

$$g^0(x, v) = \frac{1}{L} \frac{1}{\sigma \sqrt{2\pi}} e^{-\frac{v^2}{2\sigma^2}} \quad (46)$$

with $\sigma = 2$, for the δf and FBL- δf PIC methods.

6.3 Phase-space density plots

In this section we assess the accuracy and denoising capabilities of the basic δf PIC and FBL- δf PIC methods by plotting various densities in phase space. In Figures 2–9 the axes show $x \in [0, L]$ and $v \in [-v_{\max}, v_{\max}]$ with L and v_{\max} as indicated above, and the same color range is used for the purpose of comparison.

In Figures 2 and 3, we first plot the densities f^n corresponding to the different methods listed in Table 1 for both the TSI and DTSI test cases, at the time $t^n = 100$ where the exact solutions coincide.

For both test cases we observe very noisy (oscillating) profiles for the coarse full- f PIC solutions which use about 20,000 particles, and smoother profiles for the fine PIC solutions which use 16 times as many particles. FBL solutions are essentially free of spurious oscillations, with many fine structures well resolved in the fine solutions compared to the coarse ones. We also note that the TSI and DTSI solutions are in very good agreement at $t^n = 100$ for these full- f numerical simulations.

Regarding the δf solutions, we observe that in the TSI test case (Fig. 2) both the basic δf PIC and the FBL- δf PIC methods allow to strongly reduce the level of oscillations compared to the coarse PIC simulation – all three using approximately 20,000 ‘active’ particles. In the DTSI case however (Fig. 3), we see a significant reduction in the accuracy of the basic δf solution, where the global central vortex suffers from a visible deterioration and spurious streams of particles have appeared at high-velocities. In contrast, the accuracy of the FBL- δf PIC method in the DTSI case remains very comparable to that of the TSI case. In particular we observe that the new method is able to capture several low-density filaments, i.e., fine regions with zero or very low density distinct from the central vortex. In the basic δf simulation these fine structures are poorly resolved, as we can see from Fig. 3 where the low-density filaments on the left of the central vortex are virtually merged with the latter. To better visualize the difference in the two methods, we next show in Figures 4 to 9 a series of plots corresponding to

snapshots of various densities at successive times $t^n = 0, 12.5, \dots, 87.5$ for the DTSI test case: In Figure 4 and 5 we show the evolution of the δf and FBL- δf solutions, completed by that of a reference scheme (an FBL simulation using a 1024×1024 grid) in Figure 6. In Figure 7 we then show the evolution of the bulk density f_*^n computed by the FBL- δf PIC method, which we remind is periodically remapped on a 50×50 grid of cubic splines, see Table 1. Finally the evolution of the residual δf^n densities are shown in Figure 8 for the basic δf method, and in Figure 9 for the FBL- δf method.

From these plots we see that the density strongly deviates from its initial value due to the external drive, which clearly challenges the basic assumption of a standard δf approach. Here, we have chosen a deviation so large that the bulk density cannot be compensated by a proper δf weighting of the particles, leading to significant errors in the full f^n density visible in Figure 4. As expected the solution computed with the FBL- δf PIC method on Fig. 5 does not show this erratic behaviour. The main reason for this is visible in Fig. 7 where we see that the coarse bulk density computed by the FBL- δf scheme properly follows the total density. As a result the δf particles can effectively represent small scale variations with respect to the main part of the plasma density. This is made evident in Fig. 8 and 9 where we see that the amplitude of the δf particle density for the FBL- δf scheme is significantly lower than with a basic δf method.

In Fig. 7 we also observe that the numerical bulk density is subject to a visible numerical diffusion. This is an expected consequence of the periodic coarse-grid interpolations involved in the semi-Lagrangian updates, and over moderate times it should not pose a serious issue since the total density is described by the sum of the bulk and the perturbed particle density. Over long simulation times however, this numerical diffusion will lead to bulk densities that do not approximate well the total f . In such cases a proper re-initialization of the bulk density f_* will have to be devised, based on the available representation of the total density, and various methods do exist in this direction such as adaptive kernel density estimation algorithms [35, 17, 37] or adaptive sparse-grid methods [28]. We note that such an algorithm is likely be more costly than a simple update of the coarse bulk density, but this should be mitigated by the fact that it will be applied on much larger time periods.

6.4 Density and field plots in physical space

In Figures 10 and 11 we next plot the snapshots of the deposited charge densities ρ^n for the DTSI test case, corresponding to the δf and FBL- δf solutions shown in in Figures 4 and 5. For a better assessment of the accuracy, we also plot in dashed line a reference charge density computed by a fine semi-Lagrangian scheme. The associated E^n fields are plotted in Figures 12 and 13.

These plots show that despite the velocity averaging, the high level of noise visible in the δf phase-space densities is also present in the deposited charge densities, which results in significant errors in the self-consistent electric field.

6.5 Approximation of momentum and energy

We next assess the accuracy of the different methods in approximating the system momentum and energy, namely

$$\int_{\Omega} v f(z) dz \quad \text{and} \quad \frac{1}{2} \int_{\Omega} v^2 f(z) dz + \frac{1}{2} \int_0^L E(x)^2 dx$$

with $z = (x, v) \in \Omega = [0, L] \times [-v_{\max}, v_{\max}]$ as above. In Figure 14 we plot the time evolution of these discrete quantities for the TSI test-case, where they are invariants of the exact solution (assuming $f = 0$ for $|v| > v_{\max}$). The first finding is that both the full- f PIC and the FBL scheme (for the coarse and fine meshes) preserve these quantities with very good accuracy, while visible errors accumulate for the two δf methods. More precisely, we observe oscillating errors for both δf schemes, with no clear winner: although the oscillations are clearly of larger amplitude with the basic δf scheme, a secular growth is visible on the numerical energy for the FBL- δf method, which may be due to the numerical diffusion of the bulk density (visible in Fig. 7) caused by the periodic coarse updates as discussed above. We note however that for the TSI test-case both δf schemes did also show similar accuracy in the density plots of Fig. 2, so that their similar performance in the conservation properties may not come as a big surprise.

For the DTSI test-case the total momentum and energy are no longer system invariants due to the external drive. To compare the performances of the different methods we thus plot in Figure 15 the energy of the self-consistent electric field, for both the TSI (left) and DTSI (right) test-cases. Here the first observation is that the results present a high level of variability for the different methods. However, not all methods perform equally. If we consider that in both test-cases the fine FBL method (purple curve) can be used as reference, then we find that the curves of the FBL- δf scheme (in red) are of reasonable accuracy. More precisely they are less damped than those of the coarse FBL scheme (in green), and they show less oscillations than those of the coarse full- f PIC scheme (in blue). In the TSI test-case the curve of the basic δf scheme (in orange) shows a similar behaviour with slightly more oscillations, while in the DTSI test case the oscillations are of very high amplitude (close to the actual level of the energy itself). As a result, we thus find that for the DTSI test-case the new scheme also shows a superior accuracy in terms of energy approximation.

6.6 Reduction of the statistical errors

We conclude our numerical experiments by considering the empirical variances for the total particle number and current, as defined by Equations (4.80) and (4.81) in Ref. [19], namely

$$\sigma_N^2 = \frac{N_p^2}{N_p - 1} \left[\sum_{k=1}^{N_p} (\delta w_k)^2 - \left(\sum_{k=1}^{N_p} \delta w_k \right)^2 \right] \quad (47)$$

and

$$\sigma_J^2 = \frac{N_p^2}{N_p - 1} \left[\sum_{k=1}^{N_p} (v_k \delta w_k)^2 - \left(\sum_{k=1}^{N_p} v_k \delta w_k \right)^2 \right] \quad (48)$$

respectively. We note that here the weight normalisation differs from that of Ref. [19]: for δf and full- f simulations (where the weights are constant) we have

$$\delta w_k^n \approx \frac{1}{N_p} \frac{\delta f^n(z_k)}{g^n(z_k)} \quad \text{and} \quad w_k^n = w_k^0 = \frac{1}{N_p} \frac{f^0(z_k)}{g^0(z_k)},$$

respectively, see (23) and (12). In particular $\sigma_N = 0$ for full- f runs using a sampling distribution $g^0 = f^0 / (\int f^0(z) dz)$.

Following the interpretation of the δf method as a variance reduction technique [2], these respective quantities may be used as quantitative indicators of the statistical errors associated with

the Monte Carlo approximation of the total density $\iint f(t, x, v) dx dv$ and normalized current $\iint f(t, x, v)v dx dv$, see Ref. [19, Sec. 2].

In Figure 16, we plot these quantities for the two test cases, and for the three coarse PIC schemes, namely the coarse full- f PIC, the basic δf and the FBL- δf scheme. For the TSI test case corresponding to the top plots, we observe that the δf schemes indeed result in a reduction of the current variance σ_J , of a factor between two and three (the full- f density variance is zero as previously noticed). We also note a secular growth in the case of the FBL- δf scheme: this is probably due to the slow diffusion of the bulk density caused by the periodic remappings, and should be mitigated by proper re-initialization methods for the bulk density. We refer to the perspective section below for a discussion on possible improvements.

For the DTSI test case, we observe similar values for the current variances σ_J of the full- f FBL- δf PIC simulations (with values around 20 and 10, respectively). In contrast, strong oscillations are visible in the variances of the basic δf PIC scheme, which are closely correlated with the deviation in velocity already seen in Figure 4, and the associated offset with the initial density. The amplitude of these oscillations (around 40) confirm our previous observations that a basic δf approach is no longer justified when the density deviates significantly from its initial profile, and further validates the proposed method in such regimes.

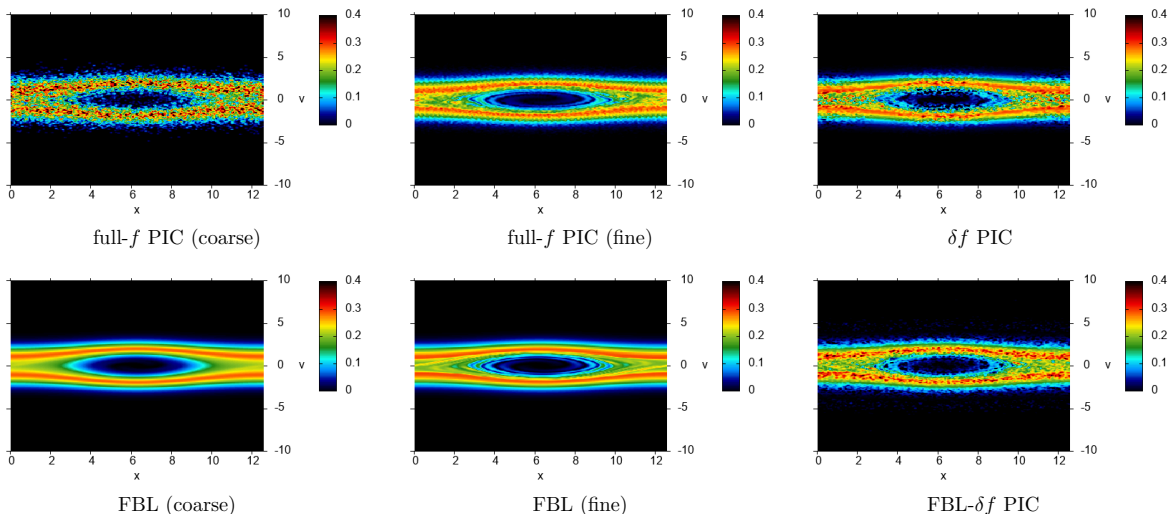


Figure 2: Phase-space densities f^n obtained for the TSI test case at $t^n = 100$ with the methods listed in Table 1. Here the basic δf and FBL- δf methods use about 18,750 standard particles and 1,250 FBL markers, which is comparable to the 20,000 particles (or active markers) used in the coarse PIC and FBL methods. Fine PIC and FBL simulations use 16 as many particles.

7 Conclusion

7.1 Summary

In this article we have presented a δf PIC method where the bulk density is represented by smooth B-splines on a coarse grid, and periodically updated with a forward-backward Lagrangian (FBL) method. This method amounts in updating the spline coefficients of the bulk density

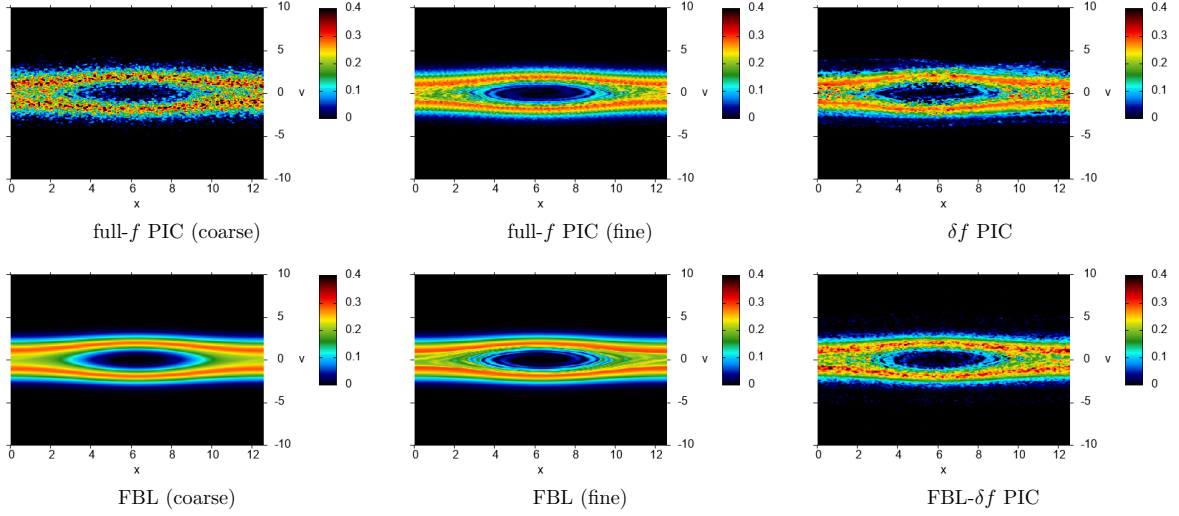


Figure 3: Densities obtained for the DTSTI test case at $t^n = 100$, where the exact solution coincides with the TSI one. As in Fig. 2, the different methods are those listed in Table 1.

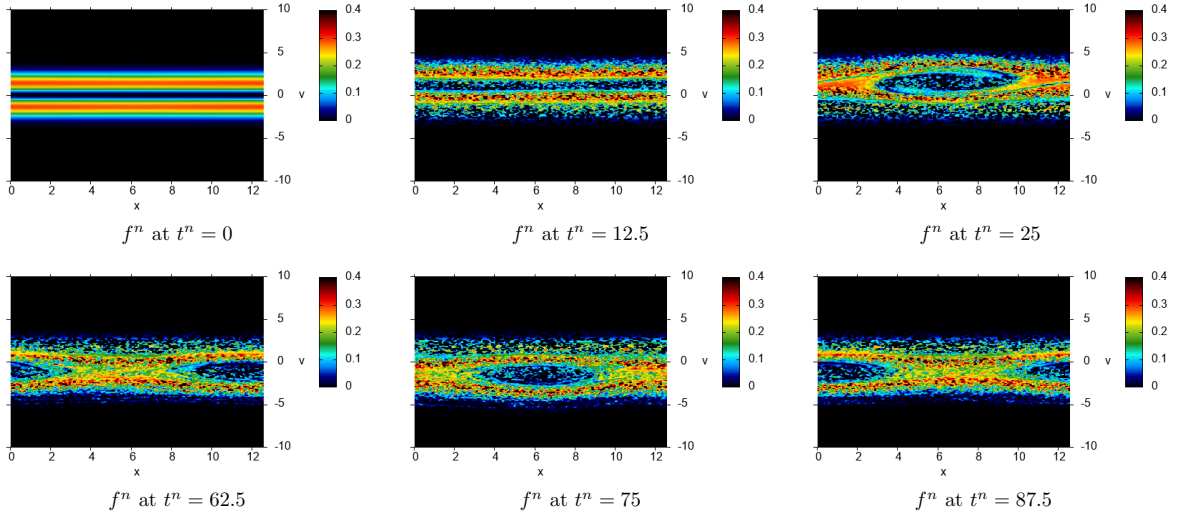


Figure 4: Snapshots of the density f^n computed by the δf PIC scheme at various times t^n , for the DTSTI test case. At time $t^n = 100$, the corresponding density is shown in the upper-right plot of Fig. 3.

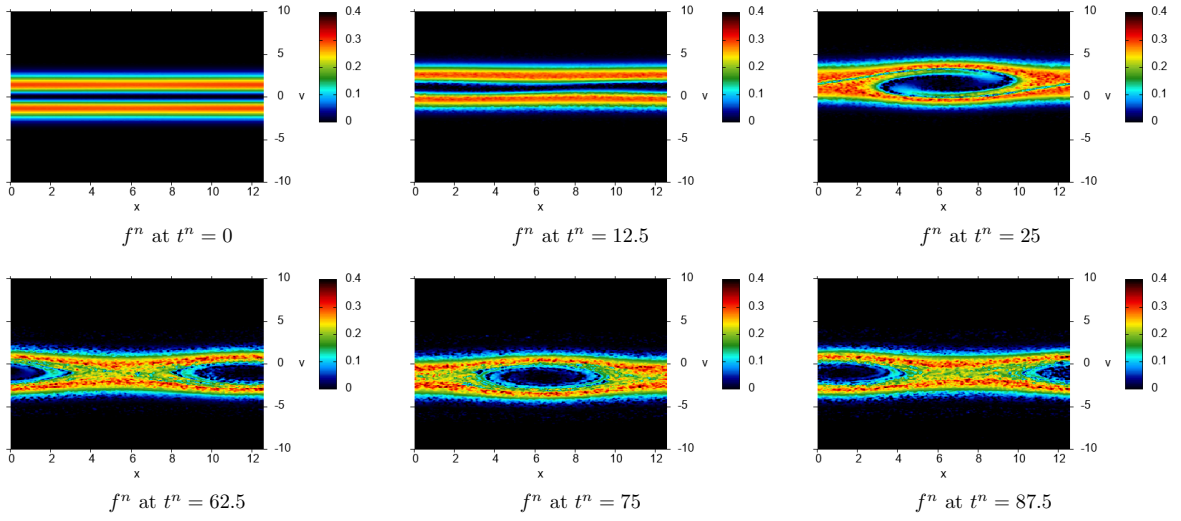


Figure 5: Snapshots of the density f^n computed by the FBL- δf PIC scheme at various times t^n , for the DTSI test case. At time $t^n = 100$, the corresponding density is shown in the lower-right plot of Fig. 3.

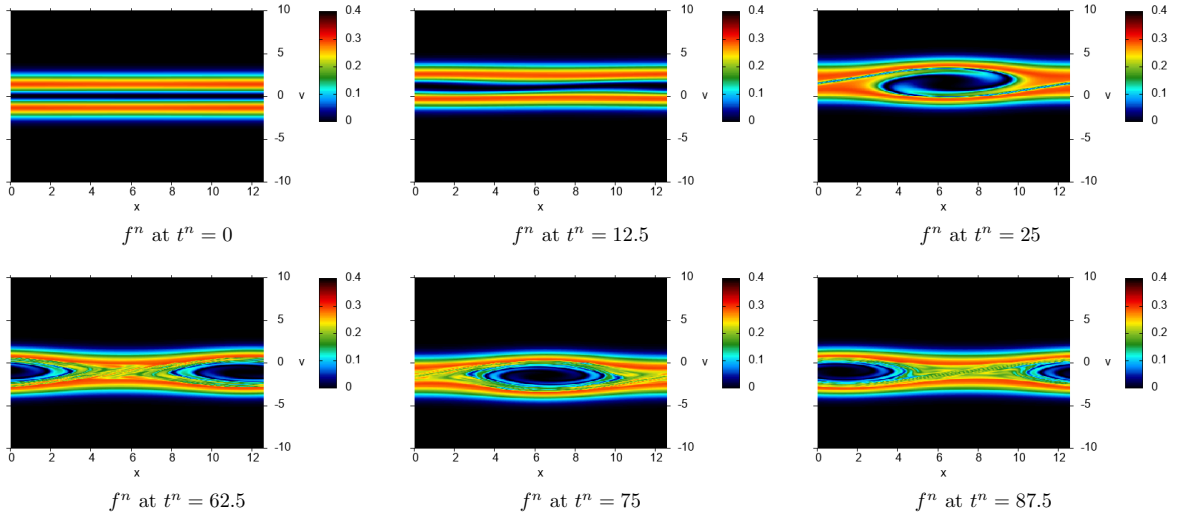


Figure 6: Snapshots of the density f^n obtained with a reference method (an FBL simulation using a 1024×1024 grid) for the same times than in Figures 4 and 5, again for the DTSI test case.

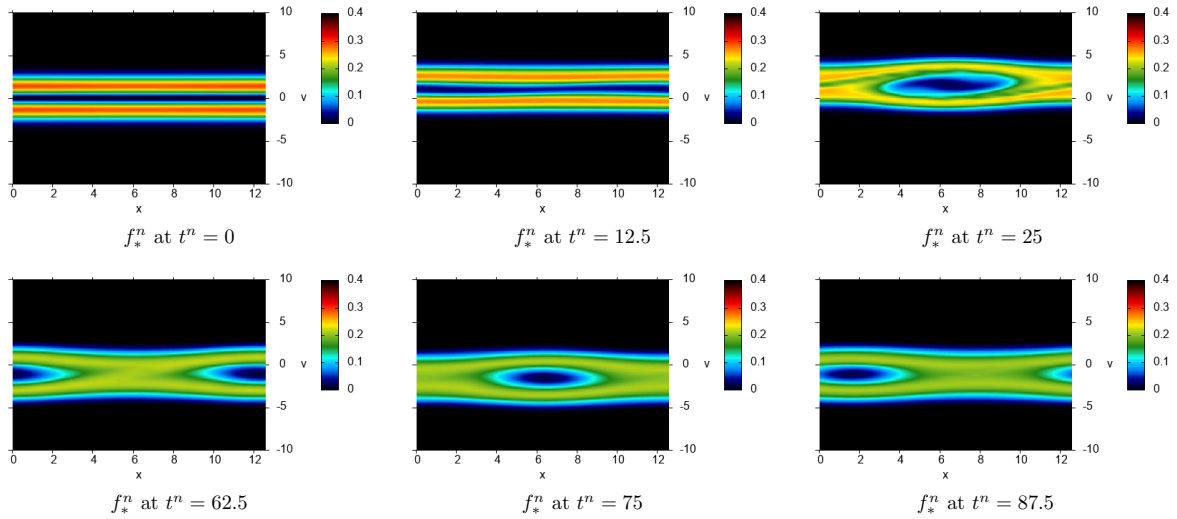


Figure 7: Snapshots of the bulk density f_*^n corresponding to the FBL- δf PIC simulation shown in Figure 5.

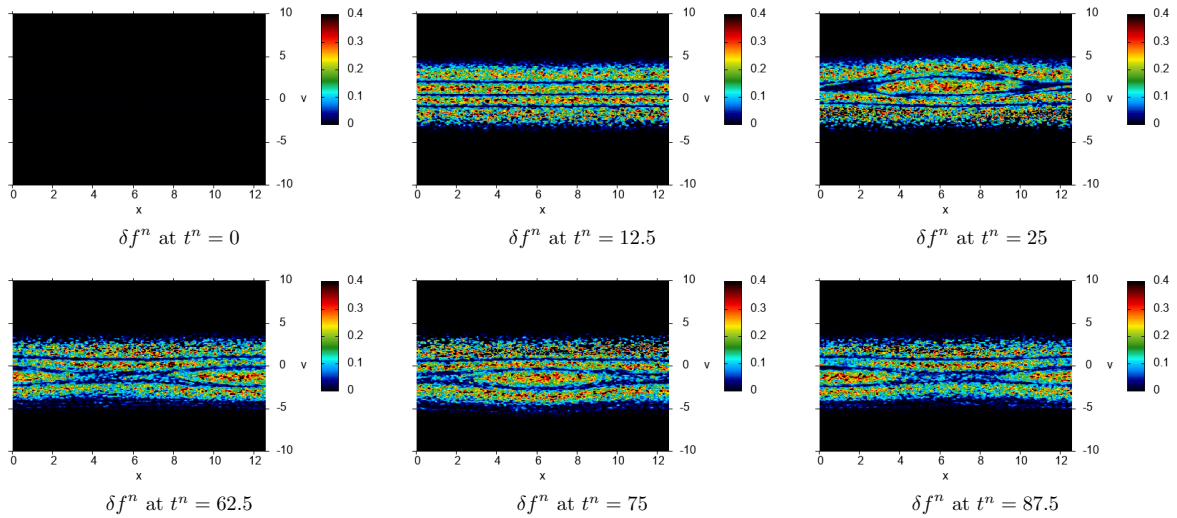


Figure 8: Snapshots of the residual density δf^n corresponding to the δf PIC simulation shown in Figure 4.

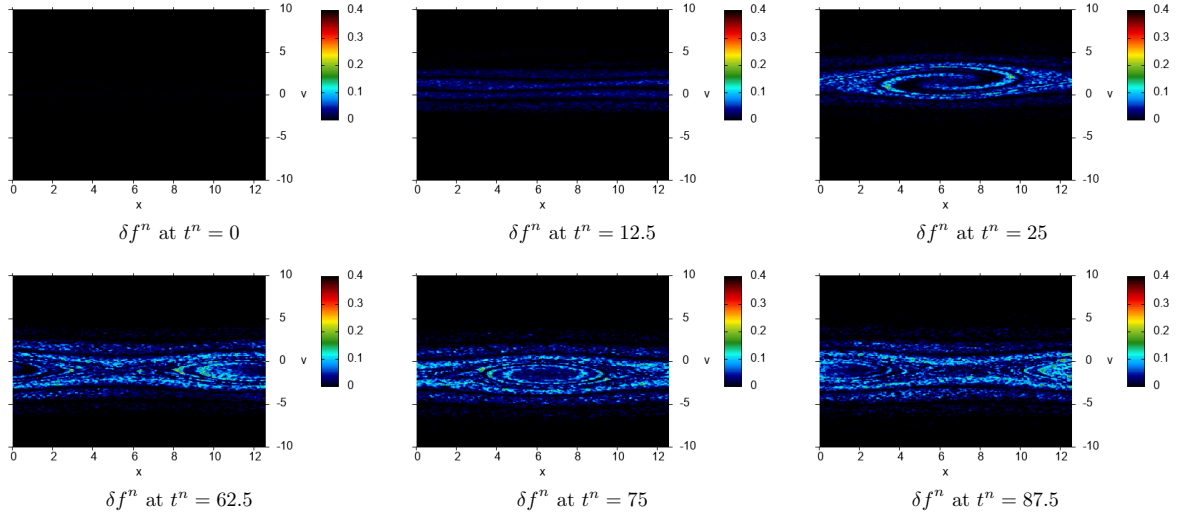


Figure 9: Snapshots of the residual density δf^n corresponding to the FBL- δf PIC simulation shown in Figure 5.

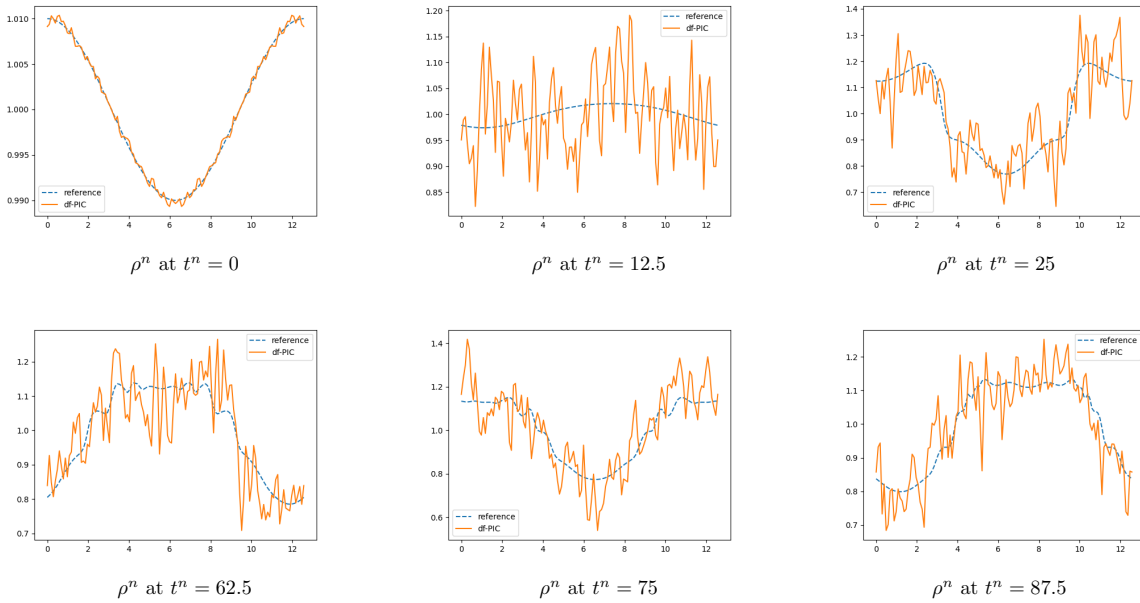


Figure 10: Snapshots of the charge density ρ^n deposited with the δf PIC scheme (with the DTSI test case), corresponding to the phase-space densities shown in Figure 4.

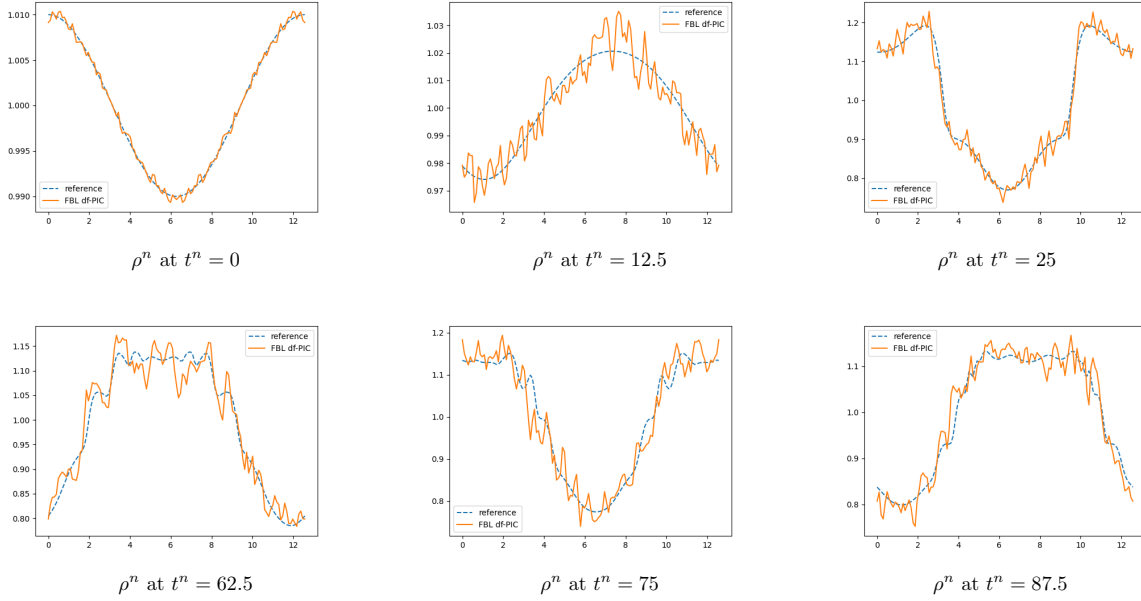


Figure 11: Snapshots of the charge density ρ^n deposited with the FBL- δf PIC scheme (with the DTSI test case), corresponding to the phase-space densities shown in Figure 5.

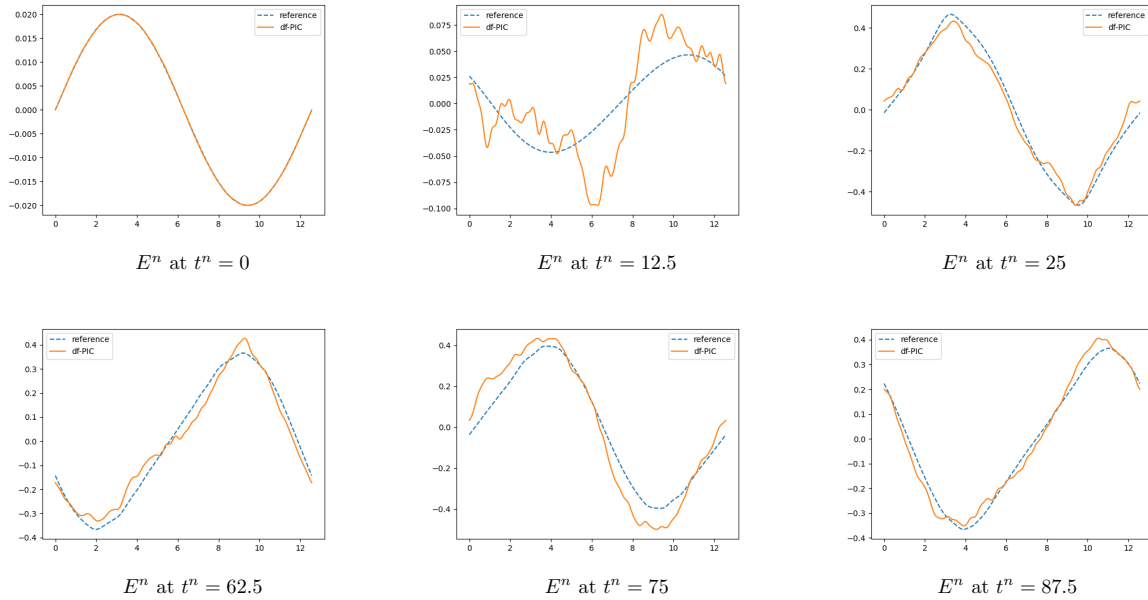


Figure 12: Snapshots of the self-consistent field E^n computed by the δf PIC scheme (DTSI), corresponding to the charge densities shown in Figure 10.

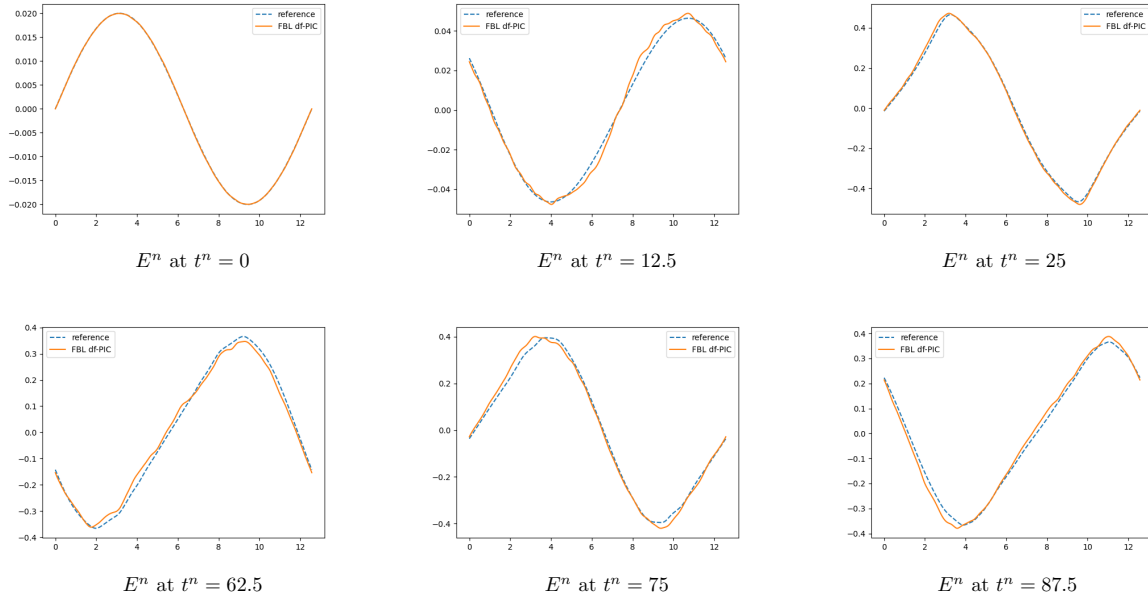


Figure 13: Snapshots of the self-consistent field E^n computed by the FBL- δf PIC scheme (DTSI) corresponding to the charge densities shown in Figure 11.

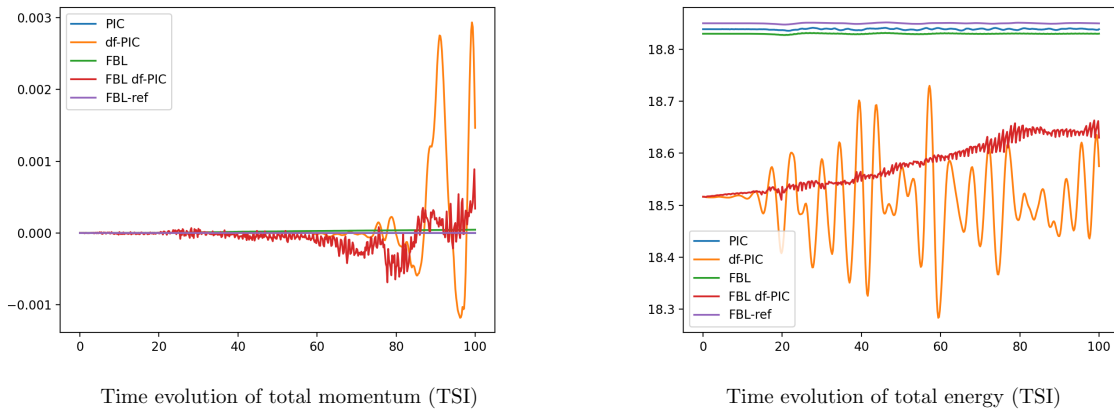


Figure 14: Time evolution of the total momentum (left) and energy (right) for the TSI test case.

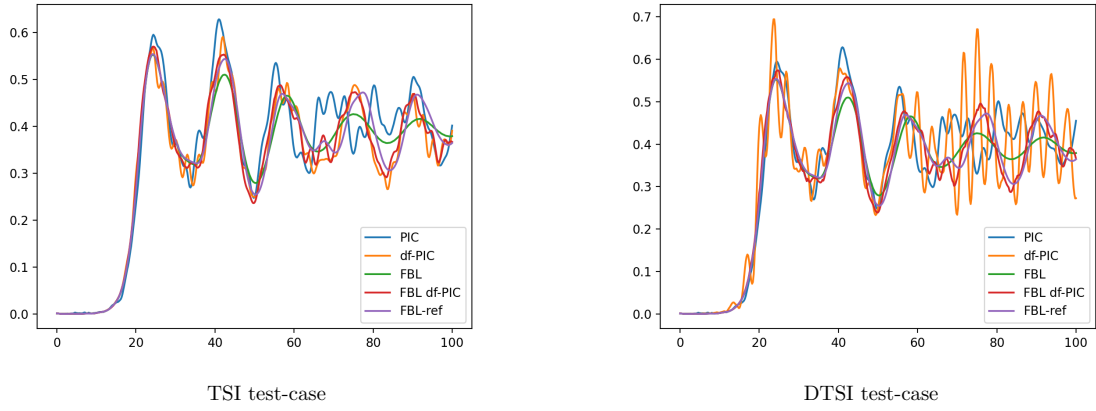


Figure 15: Time evolution of the self-consistent electric energy for the TSI (left) and DTSI (right) test cases.

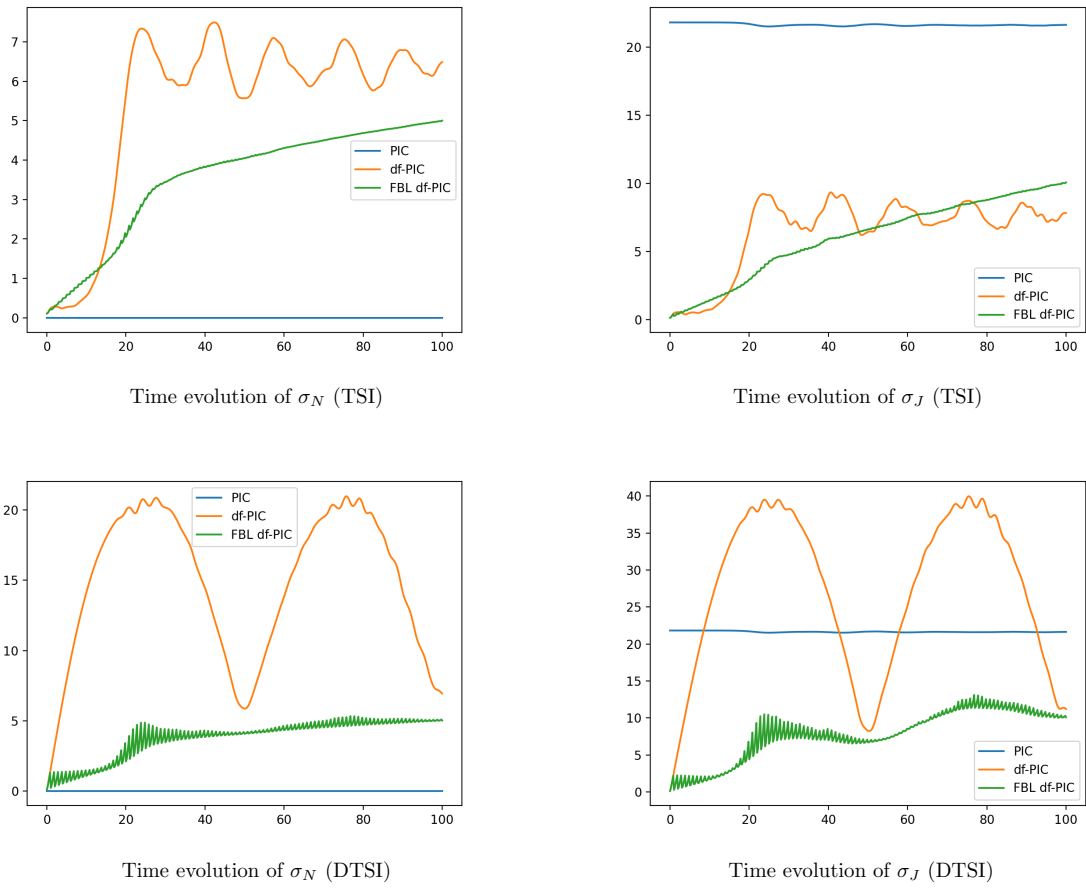


Figure 16: Time evolution of the empirical variances for the TSI (top row) and DTSI (bottom row) test cases.

with a backward semi-Lagrangian method, where the backward trajectories are obtained by local inversions of the forward trajectories provided by the PIC code. In these inversions the local backward flow is represented as a quadratic mapping whose Jacobian and Hessian matrices are computed from the relative displacements of regular passive markers pushed forward by the PIC code. After describing the representation of the bulk and variation density in terms of weighted collections of shape functions with variable width, and recalling the general form of full- f and δf particle approximations to transport problems, we have provided a detailed description of a remapped δf scheme where the bulk density updates are performed using the FBL method. Finally we have studied the basic performances of the method on two academic examples involving one-dimensional (i.e., 1D1V phase-space) electrostatic problems: a simple two stream instability where the deviation from the initial density is mild and does not justify any update of the bulk density, and a driven one where an oscillating electric field induces strong displacements of the phase-space density in velocity. In this latter case the basic equilibrium / deviation separation assumption is no longer valid and the δf method fails as expected to correctly resolve the solution. In contrast, the FBL- δf method shows good results, and a measurable reduction of the statistical error.

7.2 Novelty of the proposed approach

Although we did not compare the numerical performances of our method with the direct projection scheme of Ref. [1], we believe that opting for semi-Lagrangian updates of the bulk density is a significant novelty which has the key feature that it does not rely on an accurate particle approximation of the total density, but rather on the accurate particle *trajectories*. Two typical configurations may illustrate why this difference is meaningful: the first one is a regime where a localised plasma blob moves through an otherwise empty phase-space. In a region crossed by the blob, the bulk density should ideally go from zero to some positive density, and then go back to zero as the blob leaves the region. With a direct projection scheme however this cannot happen: as the δf particles enter the region the bulk density will be updated by their coarse projection and take a positive value, but as they leave they will not be able to exactly compensate the smooth bulk density (and neither will their projection), because they have precisely *moved away* from it. As a result the updated bulk density will retain a spurious residual of that fine discrepancy, which will remain there since the δf particles have now left. Another problematic scenario is the opposite one, where both the density and the transport flow are smooth in phase space. If the bulk density grid is not too coarse, then one will always find some phase-space cells devoid of markers: on such cells the projected δf density will be zero by construction, leading to strong oscillations. Because the forward-backward Lagrangian approach relies on the particle trajectories and a smooth grid-based bulk density, it is exempt of both these pitfalls: For the case of a moving blob this has already been seen on the DTSI test-case where the external drive moves the plasma density over large portions of the phase-space, with Fig. 7 showing a clean transport of the bulk density (e.g. between times $t^n = 0$ and 25). For the second one the key point is that a smooth flow leads to accurate backward trajectories, according to the analysis of Ref. [7]. On every grid node the new value will thus correspond to that of the previous bulk density at a point where the smooth spline density should be also accurate, independent of the markers resolution.

We also point out that this approach not only allows to approximate general bulk densities, but it can be applied to other representations, as long as their evaluation is easily computable:

instead of B-splines, one could for instance use piecewise polynomials or a collection of Fourier modes. The semi-Lagrangian updates would then involve specific algorithms (such as interpolation or FFT) for updating the weights, based on nodal evaluations of the previous density at the feet of the backward characteristics computed by the FBL scheme.

7.3 Perspectives

Moving forward, an important direction of research is to extend the present method to more challenging problems, such as higher dimensional ones. We are in particular interested in gyrokinetic models where the transport phase-space has typically 4 dimensions. In their current form the various algorithms (namely, the FBL flow reconstruction and the spline quasi-interpolation) can be directly applied to a 4D phase space, however preliminary numerical simulations have shown that typical transport flows in higher dimensions have an anisotropic smoothness which is not well captured by our isotropic algorithms. Our plan is thus to design extensions of the current approach that will be able to efficiently reconstruct high-dimensional characteristic flows with anisotropic smoothness.

Another improvement will be to design good re-initialization schemes for the bulk density that could be applied on larger time scales to counter the numerical diffusion inherent to the coarse semi-Lagrangian updates, as well as the secular growths in the energy error and in the variance, observed in Fig. 14 and 16. Adaptive approximation methods do exist which have already shown good results for particle denoising, such as adaptive wavelet or Fourier filters [35, 17] kernel density estimation algorithms [37] which automatically select the optimal width for the particle shape functions, or sparse-grid adaptive methods [28] which have also proven effective for particle denoising in higher dimensions.

Acknowledgments

The authors thank Roman Hatzky for fruitful discussions on statistical error reduction, as well as the anonymous reviewers for their comments which have improved the presentation of our results. This work has been carried out within the framework of the EUROfusion Consortium and has received funding from the Euratom research and training programme 2014-2018 and 2019-2020 under grant agreement No 633053. The views and opinions expressed herein do not necessarily reflect those of the European Commission.

References

- [1] S J Allfrey and R Hatzky. A revised δf algorithm for nonlinear pic simulation. *Computer Physics Communications*, 154(2):98–104, Aug 2003.
- [2] A. Y. Aydemir. A unified monte carlo interpretation of particle simulations and applications to non-neutral plasmas. *Physics of Plasmas*, 1(4):822–831, April 1994.
- [3] A Biancalani, A Bottino, A Di Siena, Ö Gürçan, T Hayward-Schneider, F Jenko, P Lauber, A Mishchenko, P Morel, I Novikau, F Vannini, L Villard, and A Zocco. Gyrokinetic investigation of Alfvén instabilities in the presence of turbulence. *Plasma Physics and Controlled Fusion*, 63(6):065009, June 2021.

- [4] C K Birdsall and A.B. Langdon. *Plasma physics via computer simulation*. Adam Hilger, IOP Publishing. Adam Hilger, IOP Publishing, 1991. Original Version: McGraw-Hill, New York, 1985.
- [5] G. Brochard, R. Dumont, H. Lütjens, and X. Garbet. Linear stability of the ITER 15 MA scenario against the alpha fishbone. *Nuclear Fusion*, 60(8):086002, June 2020. Publisher: IOP Publishing.
- [6] Indra C, Ario Yudo Husodo, Wisnu Jatmiko, Budi Wiweko, Alfred Boediman, and Beno K. Pradekso. Denoising Noisy ECG Signal Based on Adaptive Fourier Decomposition. In *2018 3rd International Seminar on Sensors, Instrumentation, Measurement and Metrology (ISSIMM)*, pages 11–14, December 2018.
- [7] Martin Campos Pinto and Frédérique Charles. From particle methods to forward-backward Lagrangian schemes. *SMAI Journal of Computational Mathematics*, 4:121–150, 2018.
- [8] Yang Chen and Scott E Parker. Coarse-graining phase space in δf particle-in-cell simulations. *Physics of Plasmas*, 14(8):2301, August 2007.
- [9] C Z Cheng and G Knorr. The integration of the vlasov equation in configuration space. *Journal of Computational Physics*, 22:330–351, Nov 1976.
- [10] C.K. Chui and H. Diamond. A characterization of multivariate quasi-interpolation formulas and its applications. *Numerische Mathematik*, 57(1):105–121, 1990.
- [11] Stéphane Colombi and Christophe Alard. A ‘metric’ semi-Lagrangian Vlasov–Poisson solver. *Journal of Plasma Physics*, 83(3):1–28, June 2017.
- [12] Stéphane Colombi and Christophe Alard. A ‘metric’ semi-Lagrangian Vlasov–Poisson solver. *Journal of Plasma Physics*, 83(3):705830302, June 2017. Publisher: Cambridge University Press.
- [13] G. Dif-Pradalier, G. Hornung, Ph. Ghendrih, Y. Sarazin, F. Clairet, L. Vermare, P.H. Diamond, J. Abiteboul, T. Cartier-Michaud, C. Ehrlacher, D. Estève, X. Garbet, V. Grandgirard, Ö.D. Gürçan, P. Hennequin, Y. Kosuga, G. Latu, P. Maget, P. Morel, C. Norcini, R. Sabot, and A. Storelli. Finding the Elusive $E \times B$ Staircase in Magnetized Plasmas. *Physical Review Letters*, 114(8):085004, February 2015.
- [14] A. M. Dimits and W. W. Lee. Partially linearized algorithms in gyrokinetic particle simulation. *Journal of Computational Physics*, 107(2):309–323, 1993.
- [15] Mikhail Dorf and Milo Dorr. Progress with the 5D full-F continuum gyrokinetic code COGENT. *Contributions to Plasma Physics*, 60(5-6):e201900113, 2020. eprint: <https://onlinelibrary.wiley.com/doi/pdf/10.1002/ctpp.201900113>.
- [16] Francis Filbet and E. Sonnendrücker. Comparison of eulerian vlasov solvers. *Computer Physics Communications*, 150(3):247–266, 2003.
- [17] You Gao, Min Ku, Tao Qian, and Jianzhong Wang. FFT formulations of adaptive Fourier decomposition. *Journal of Computational and Applied Mathematics*, 324:204–215, November 2017.

- [18] V. Grandgirard, J. Abiteboul, J. Bigot, T. Cartier-Michaud, N. Crouseilles, G. Dif-Pradalier, Ch. Ehrlacher, D. Esteve, X. Garbet, Ph. Ghendrih, G. Latu, M. Mehrenberger, C. Norscini, Ch. Passeron, F. Rozar, Y. Sarazin, E. Sonnendrücker, A. Strugarek, and D. Zarzoso. A 5D gyrokinetic full-f global semi-Lagrangian code for flux-driven ion turbulence simulations. *Computer Physics Communications*, 207:35–68, October 2016.
- [19] R. Hatzky, R. Kleiber, A. Könies, A. Mishchenko, M. Borchardt, A. Bottino, and E. Sonnendrücker. Reduction of the statistical error in electromagnetic gyrokinetic particle-in-cell simulations. *Journal of Plasma Physics*, 85(1):905850112, Feb 2019.
- [20] Roman Hatzky, Trach Minh Tran, Axel Könies, Ralf Kleiber, and Simon J. Allfrey. Energy conservation in a nonlinear gyrokinetic particle-in-cell code for ion-temperature-gradient-driven modes in θ -pinch geometry. *Physics of Plasmas*, 9(3):898–912, 2002.
- [21] R.W. Hockney and J.W. Eastwood. *Computer simulation using particles*. Taylor & Francis, Inc, Bristol, PA, USA, 1988.
- [22] M. Kotschenreuther. Numerical simulation. In *Bulletin of the American Physical Society*, volume 33, page 2017, 1988.
- [23] E. Lanti, N. Ohana, N. Tronko, T. Hayward-Schneider, A. Bottino, B. F. McMillan, A. Mishchenko, A. Scheinberg, A. Biancalani, P. Angelino, S. Brunner, J. Dominski, P. Donnel, C. Gheller, R. Hatzky, A. Jocksch, S. Jolliet, Z. X. Lu, J. P. Martin Collar, I. Novikau, E. Sonnendrücker, T. Vernay, and L. Villard. Orb5: A global electromagnetic gyrokinetic code using the PIC approach in toroidal geometry. *Computer Physics Communications*, 251:107072, June 2020.
- [24] C.L. Lawson and R.J. Hanson. *Solving Least Squares Problems*. Society for Industrial and Applied Mathematics, May 2012.
- [25] N. R. Mandell, A. Hakim, G. W. Hammett, and M. Francisquez. Electromagnetic full-gyrokinetics in the tokamak edge with discontinuous Galerkin methods. *Journal of Plasma Physics*, 86(1):905860109, February 2020. Publisher: Cambridge University Press.
- [26] A. Mishchenko, A. Bottino, R. Hatzky, E. Sonnendrücker, R. Kleiber, and A. Könies. Mitigation of the cancellation problem in the gyrokinetic particle-in-cell simulations of global electromagnetic modes. *Physics of Plasmas*, 24(8):081206, Aug 2017.
- [27] Alexey Mishchenko, Roman Hatzky, and Axel Könies. Conventional δf -particle simulations of electromagnetic perturbations with finite elements. *Physics of Plasmas*, 11(12):5480–5486, 2004.
- [28] Sriramkrishnan Muralikrishnan, Antoine J. Cerfon, Matthias Frey, Lee F. Ricketson, and Andreas Adelman. Sparse grid-based adaptive noise reduction strategy for particle-in-cell schemes. *Journal of Computational Physics: X*, 11:100094, June 2021.
- [29] S. E. Parker and W. W. Lee. A fully nonlinear characteristic method for gyrokinetic simulation. *Physics of Fluids B: Plasma Physics*, 5(1):77–86, 1993.
- [30] P.-A. Raviart. An analysis of particle methods. In *Numerical methods in fluid dynamics (Como, 1983)*, pages 243–324. Lecture Notes in Mathematics, Berlin, 1985.

- [31] B. Rettino, T. Hayward-Schneider, A. Biancalani, A. Bottino, Ph. Lauber, I. Chavdarovski, M. Weiland, F. Vannini, and F. Jenko. Gyrokinetic modeling of anisotropic energetic particle driven instabilities in tokamak plasmas. *Nuclear Fusion*, 62(7):076027, July 2022.
- [32] James A Rossmannith and David C Seal. A positivity-preserving high-order semi-Lagrangian discontinuous Galerkin scheme for the Vlasov-Poisson equations. *Journal of Computational Physics*, 230(16):6203 – 6232, 2011.
- [33] E. Sonnendrücker, J. Roche, P. Bertrand, and A. Ghizzo. The semi-Lagrangian method for the numerical resolution of the Vlasov equation. *Journal of Computational Physics*, 149(2):201–220, 1999.
- [34] E. Sonnendrücker, Abigail Wachter, Roman Hatzky, and Ralf Kleiber. A split control variate scheme for PIC simulations with collisions. *Journal of Computational Physics*, 295:402–419, August 2015.
- [35] Romain Nguyen van yen, Diego del Castillo-Negrete, Kai Schneider, Marie Farge, and Guangye Chen. Wavelet-based density estimation for noise reduction in plasma simulations using particles. *Journal of Computational Physics*, 229(8):2821–2839, April 2010.
- [36] T. Vernay, S. Brunner, L. Villard, B. F. McMillan, S. Jolliet, T. M. Tran, A. Bottino, and J. P. Graves. Neoclassical equilibria as starting point for global gyrokinetic microturbulence simulations. *Physics of Plasmas*, 17(12):122301, 2010.
- [37] Wentao Wu and Hong Qin. Reducing noise for PIC simulations using kernel density estimation algorithm. *Physics of Plasmas*, 25(10):102107, October 2018. Publisher: American Institute of Physics.